arXiv:1511.08534v1 [astro-ph.EP] 27 Nov 2015

Manuscript for *Revista Mexicana de Astronomía y Astrofísica* (2007)

# 3D MODELING OF SPECTRA AND LIGHT CURVES OF HOT JUPITERS WITH PHOENIX; A FIRST APPROACH

Juan J. Jiménez-Torres,[1]

*Draft version: November 30, 2015*

RESUMEN

En este artículo, un modelo de circulación global fue empleado para alimentar el código PHOENIX para calcular espectros y curvas de luz tridimensionales de Jupiters calientes. Flujos radiativos de atmósferas con polvo y sin nubes para el planeta HD179949b fueron modelados para mostrar diferencias entre ellos. Las simulaciones con el código PHOENIX pueden explicar las propiedades generales de las curvas de luz observadas a 8 $\mu$m, incluyendo el hecho de que la razón de flujo planeta-estrella alcance su máximo antes del eclipse secundario. El espectro de transmisión calculado con PHOENIX reproduce datos observacionales a 3.6 $\mu$m y sobreestima valores a 4.5, 5.8 y 8.0 $\mu$m. Estas discrepancias provienen de la composición química y proporcionan una motivación para incorporar diferentes metalicidades en estudios futuros.

ABSTRACT

In this paper, a detailed Global Circulation Model was employed to feed the PHOENIX code to calculate 3D spectra and light curves of hot Jupiters. Cloud free and dusty radiative fluxes for the planet HD179949b were modeled to show differences between them. The PHOENIX simulations can explain the broad features of the observed 8 $\mu$m light curves, including the fact that the planet-star flux ratio peaks before the secondary eclipse. The PHOENIX reflection spectrum matches the Spitzer secondary-eclipse depth at 3.6 $\mu$m and underpredicts the eclipse depths at 4.5, 5.8 and 8.0 $\mu$m. These discrepancies result from the chemical composition and provide motivation for incorporating different metallicities in future studies.

*Key Words:* Planets and satellites: atmospheres – Planets and satellites: individual (HD179949b, HD209458b)

## 1. INTRODUCTION

A hot Jupiter is any of various extrasolar planets which is as big and gaseous as Jupiter, but is much hotter due to a very close orbit around its parent star (Seager 2010). Hot jupiter planets experience a strong irradiation from their parent stars and are expected to be tidally locked because they are very close ($< 0.05$ AU) to their host star, resulting in permanent day and nightsides (Knutson et al. 2007). The consequences of such small orbital

[1]Hamburger Sternwarte, Gojenbergsweg 112, 21029 Hamburg, Germany

separations are atmospheric structures and spectra that are very different from the giant planets in the Solar system (Barman et al. 2005).

In the literature, there are several models of spectra and light curves of hot Jupiters. The majority of these models are one dimensional (1D) codes, e.g., Burrows et al. (2006) investigated spectra and light curves of planets with various day-night effective temperature differences, assuming 1D profiles for each hemisphere. Iro et al. (2005) extended 1D models by adding heat transport due to a simple parameterization of winds to generate longitude-dependent temperature maps, but they did not compute disk-averaged spectra for these models. Barman et al.(2005) investigated two-dimensional (2D) models with axial symmetry around the planet's substellar-antistellar axis and computed infrared spectra as a function of orbital phase. These 1D and 2D radiative-convective equilibrium models have had some success in matching Spitzer observations; however, Seager et al. (2005) and Deming et al. (2006) showed that ground-based data for HD209458b do not indicate prominent flux peaks at 2.3 and 3.8 $\mu$m, which the 1D and 2D solar composition models predicted. Dobbs-Dixon & Agol (2013) presented 3D radiative-hydrodynamical models for the hot Jupiter HD189733b. To address the radiative transfer they developed a frequency dependent, two-stream approximation (Mihalas 1978) for the radial radiative flux. Their transit spectrum agrees well with the data from the infrared to the UV, though it slightly under-predicts the observations at wavelengths shorter than $\sim 0.6$ $\mu$m. Their emission spectrum agrees well at 5.8 and 8 $\mu$m, but over-predicts the emission at 3.6 and 4.5 $\mu$m. Their phase curves agree fairly well with the amplitudes of variations, shape, and phases of minimum and maximum flux. However, they over-predict the peak amplitude at 3.6 $\mu$m and 4.5 $\mu$m. Rauscher & Menou (2010) presented a 3D hot Jupiter model, extending from 200 bar to 1 mbar, using an intermediate general circulation model and adopting a physical setup nearly identical to the model of HD 209458b by Cooper & Showman (2006). Discrepancies can have their origin in the different methods of solution adopted and/or the fact the equations solved are missing some of the physics at work in the hot Jupiter context. In the hot Jupiter modeling context, Rauscher & Menou can not be certain of the accuracy and validity of their models until they can likewise produce consistent results. By using a 3D general circulation model with Newtonian cooling and dayside and nightside equilibrium temperature profiles, Burrows et al. (2010) created models for the planet HD209458b. They obtained transit radius spectra during the primary transit. With a 1D spectral atmosphere code, they integrated over the face of the planet seen by an observer at various orbital phases and calculated light curves as a function of wavelength. However, since their circulation model uses Newtonian cooling (and not radiative transfer using opacities that correspond to those used in the post-processing), their calculations could be slightly inconsistent. On their behalf, for the planets HD209458b and HD189733b, Fortney et al. (2010) computed spectra for both 1D and 3D model atmospheres and examined the differences between them.

In this paper, the 3D version of the radiative transfer PHOENIX code has been used to compute light curves as well as reflection spectra for a 3D temperature-pressure structure on a latitude and longitude grid. A suitable treatment of atmospheric dynamics, non-equilibrium chemistry, and 3D radiative transfer is a considerable improvement in this work. In this scheme, given the 3D Tempertaure-Pressure grid, with corresponding chemical mixing ratios, the PHOENIX radiative transfer scheme solves for the upward and downward fluxes in each layer. These fluxes are wavelength dependent and differ from layer to layer. The modeling of atmospheres with the PHOENIX code can be important for at least two reasons. First, since the emergent spectra of hot Jupiters are determined by the chemistry and physics of their outer atmospheres, when direct detection of hot Jupiters is achieved and spectra are obtained, PHOENIX models can be essential in the interpretation of the data and in the extraction of essential physical information such as radius, gravity, temperature, and composition. Second, theoretical spectral models are important in guiding current and upcoming direct hot Jupiter searches.

This work is organized in 3 sections: the first one provides a brief introduction to hot Jupiters and the relevance of the PHOENIX code to model planetary atmospheres. The second section provides the description of the PHOENIX code to simulate the irradiation of hot Jupiters, explains the mathematical framework to solve the radiative transfer equation by numerical methods, and also gives a description of the physics and microphysics of irradiated atmospheres. The Global Circulation Model (GCM) to generate the temperature-pressure structures to feed the 3D radiative transfer PHOENIX code is also presented in section 2. Section 3 corresponds to results; it shows radiative fluxes at interesting positions on the planet; cloud-free and dusty atmosphere models of the hot Jupiter HD179949b are presented to see the differences between them. PHOENIX cloud-free and dusty light curves were calculated in different wavelength bands and compared to actual data points. Finally, cloud-free and dusty spectra are presented for the planet HD179949b. The cloud-free PHOENIX spectrum was confronted with observational data from the hot jupiter HD209242b and it was found that the theoretical model is able to fit some planet-star flux data points.

## 2. METHODOLOGY

For calculations in this paper, the 3D radiative transfer equation is solved along rays or characteristics (see Hauschildt & Baron 2006; Olson & Kunasz 1987). The iterative method for the solution of the radiative transfer equation is the method to solve the scattering problem and is based on the philosophy of operator perturbation (Cannon 1973; Scharmer 1984). Its numerical approach is based on finding consistent solutions of the source function and the mean intensity by iterative methods. The mean intensities in this study were calculated as established in Hauschildt & Baron (2006), that is, the mean intensity $J$ is obtained from the source function $S$ by a formal solution of the

radiative transfer equation. The equation of state (EOS) calculations themselves follow the method discussed in Smith & Missen (1982), whereas the Equation of State (EOS) plus opacity setups are identical to Husser et al. (2013).

### 2.1. *The PHOENIX code*

The latest version of the PHOENIX code 10.6 has been used to calulate the mean intensities, reflection spectra and light curves of hot Jupiters. The original version of PHOENIX includes a detailed radiative transfer (Hauschildt 1992) that allows for spherical symmetry. The modeling of the effects of extremely irradiated atmospheres considers a full 3D radiation transport modeling, including deviations from the local thermodynamics equilibrium (NLTE). The treatment includes scattering, which is an important effect for the dayside of a planet due to the high temperature caused by the irradiation and near the terminator due to scattering on dust particles that can survive there due to the lower termperature. The numerical atmosphere modeling with PHOENIX includes the combination of a radiative transfer technique with atmospheric structure and boundary constraints. The PHOENIX code incorporates a 3D radiation transport framework (Hauschildt & Baron 2006; Baron & Hauschildt 2007; Hauschildt et al. 2008; Baron et al. 2009) into the PHOENIX package, creating the 3D PHOENIX mode in addition to the 1D PHOENIX mode of the PHOENIX program package (Hauschildt & Baron 2010).

Planetary atmospheres in this work are modeled in spherical coordinates whose volume is divided into discrete elements of space. Such a finite element of space is called a volume element or voxel. A single characteristic hits the voxels of the grid under different angles and thus, provides different contributions to the angular resolution of the mean intensity in the different layers. Each voxel is then assigned with physical quantities like temperature, pressure, opacity, emissivity, intensity, source function and so on, then the radiative transfer is solved inside each voxel by a numerical quadrature (see Barman et al. 2005).

### 2.2. *The Global Circulation Model*

The impact of horizontal motions on hot Jupiter atmospheres has been modeled by a variety of groups (e.g. Showman & Guillot 2002; Cho et al. 2003; Burkert et al. 2005; Cooper & Showman 2005); despite the differences in methods and results, the general consensus from these hydrodynamic simulations is that circulations can redistribute a fraction of the incident energy over large portions of a strongly irradiated planetary atmosphere.

For models in this paper, the 3D approaches to the atmospheric circulation of hot Jupiters are external models (T. Barman, 2012, private communication), that is, the Global Circulation Models in this work were generated from the model data by Showman et al. (2009), just straight from them.

They approximated the dayside heating and nightside cooling using a Newtonian cooling/heating scheme, which parameterizes the radiative heating rate (in K $s^{-1}$) as ($T_{eq}$ - T)/$\tau_{rad}$, where $T_{eq}$ is the specified radiative-equilibrium temperature profile, $T$ is the actual temperature, and $\tau_{rad}$ is the radiative-equilibrium timescale. These atmospheric circulation models are based on six fundamental conservation equations: the conservation of mass, conservation of momentum (one equation for each dimension), conservation of energy, and the ideal gas law as the equation of state. Within the context of the Newtonian cooling framework, Showman et al. (2009) calculated the longitude, latitude, and height-dependent radiative-equilibrium temperatures.

The radiative-equilibrium temperature structures described above were used as input structure files to feed the 3D radiative transfer PHOENIX code to generate models of hot Jupiters. Figure 1 illustrates the behavior for the simulation of the Showman et al. (2009) Global Circulation Model using solar opacities. It shows the temperature (colorscale) over the globe on three different pressure levels. A temperature range of 346 K to 896 K is observed on the external layer with pressure equal to $\sim 10^{-6}$ bar, indicating that the absorbed energy from the parent star is distributed through the planet's atmosphere, that is, the irradiated dayside is efficiently redistributed throughout the atmosphere. The day-night temperature differences reached nearly 40 K at 170 bar and 600 K at 20 mbar. Although the detailed structure varies between levels, the hottest regions lie east of the substellar point throughout. The atmospheric dynamics distorts the temperature pattern in a complex manner, which includes the eastward displacement of the hottest regions from the substellar point.

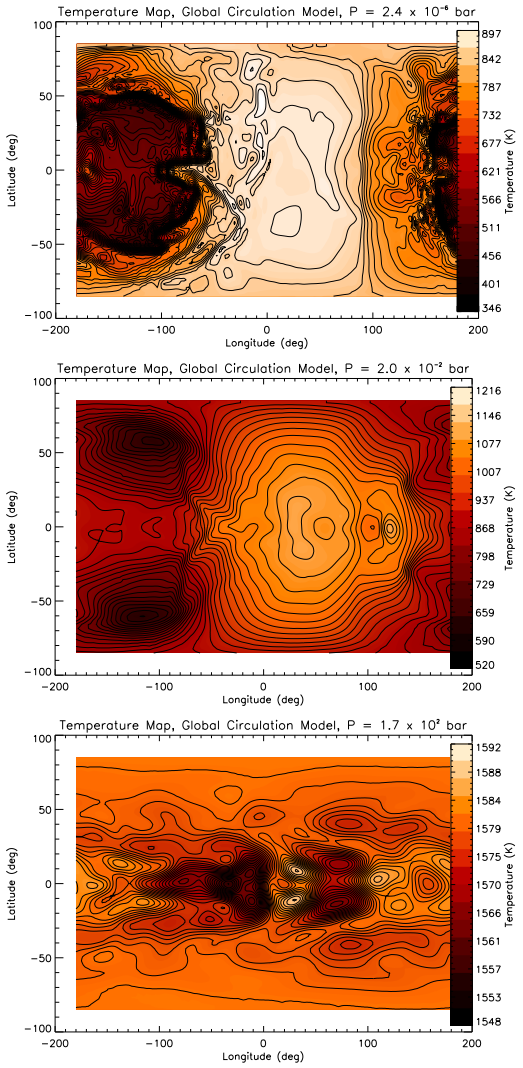
Temperature Map, Global Circulation Model, P = 2.4 x 10⁻⁶ bar
Temperature Map, Global Circulation Model, P = 2.0 x 10⁻² bar
Temperature Map, Global Circulation Model, P = 1.7 x 10² bar
Latitude (deg)
Longitude (deg)
Temperature (K)

Fig. 1. Simulated temperature maps of the Global Circulation Model. Maps use a linear scale, with the hottest points in white and the coldest points in black. From top to bottom there are three isobars: 0.0024, 20 and 170 000 mbar. The substellar point is at (0,0) in longitude and latitude. The dynamics distorts the temperature pattern in a complex manner; this generally includes an eastward displacement of the hottest regions from the substellar point.

Figure 2, illustrates a diversity of vertical temperature profiles that occur. It portrays in two panels the temperature-pressure structure profile as function of longitude. The left frame corresponds to latitude 0 degrees and the right one to 30 degrees. Solid lines correspond to different positions on the planet; magenta line corresponds to Long=-120 deg, black to Long=-90 deg, red to Long=-45 deg, blue to Long=0 deg, green to Long=45 deg, cyan to Long=60 deg and yellow to Long=90 deg. Slight bumps (on the nightside) and depressions (on the dayside) are noted between $\sim 10^1$ and $\sim 10^2$ bars in the temperature-pressure profiles, this region is near where the heat redistribution is expected to occur.

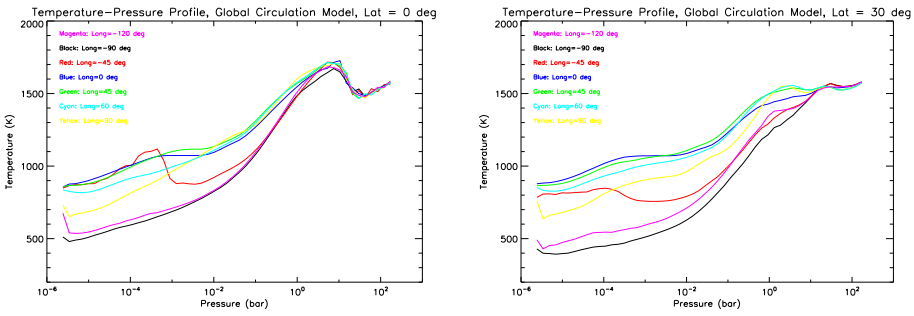


Fig. 2. A selection of temperature-pressure profiles for the solar-abundance Global Circulation Model. The equatorial region is on average warmer than the 30 deg latitude at pressures of less than a few bars. Note the formation of a stratosphere at pressures less than 0.1 bars.

As expected, the equatorial region is on average warmer than the 30 deg latitude at pressures of less than a few bars. At low pressures, longitudinal variation is comparable to the latitudinal variation. The temperature declines smoothly with altitude from $\sim 10^0$ bars to $\sim 10$ mbar. This has important implications for the spectra and light curves, which originate within this layer. Dynamics modifies the deep stable radiative layer from 10-100 bars, leading to significant latitude variation of both temperature and static stability (Showman et al. 2009). Following analysis found in Seager (2010), the Temperature-Pressure profiles shown in figure 2 could be divided into three representative layers. Above layer 1, at pressures below P $\sim 10^{-2}$, the optical depth at all wavelengths becomes low enough so that the layers of the atmosphere are transparent to the incoming and outgoing radiation and not relevant for spectral features. This uppermost layer, has no thermal inversions. The layer 2 from $\sim 10^{-2}$ bar to $\sim 10^0$ bar is where most spectral features are formed. In this layer, the temperature structure is governed by radiative process and possibly by atmospheric dynamics. These optically thin layers are at altitudes where thermal inversions may be formed. The layer 3 from $\sim 10^0$ bar to $\sim 10^2$ bar is the regime where a high optical depth leads to radiative diffusion and the related isothermal temperature structure. Below this layer, in the deepest layers of the planet atmosphere, convection is the dominant energy transport mechanism.

## 3. RESULTS

In this section theoretical radiative fluxes, light curves and reflection spectra are presented to simulate irradiated Global Circulation Models (hot Jupiters). To calculate the mean intensities, the temperature-pressure profiles described in subsection 2.2 are used as an input for the 3D radiative transfer PHOENIX code so that it can generate the radiation fields. Then this grid with $S$ (source function) and $J$ (mean intensities) is used to create 3D visualizations (spectro-images), spectra and light curves. In this study, the Global Circulation Model passing in front of its parent star is simulated with PHOENIX on a 3.5M

TABLE 1

PHYSICAL AND ORBITAL PARAMETERS OF THE PLANETARY SYSTEM HD179949 (COWAN ET AL. (2007); BURROWS ET AL. 2008)).

| Planet | a(AU) | Star | $R_\star(R_\odot)$ | Teff(K) | $M_\star(M_\odot)$ | $L_\star(L_\odot)$ |
|---|---|---|---|---|---|---|
| HD 179949b | 0.045 | HD 179949 | 1.24 | 6200 | 1.24 | 2.0 |

voxels grid with $n_r = 53$, $n_\theta = 257$ and $n_\phi = 257$ voxels. This number of voxels was selected to be large enough to minimize the effects of pixellation but small enough to give reasonable computation times. The irradiated models presented in this section were computed using the PHOENIX atmosphere code (Hauschildt & Baron 1999; Allard et al. 2001) adapted to include extrinsic radiation as described in Barman et al. (2001; 2002).

### 3.1. *Test radiative fluxes*

Experiments in this subsection corresponds to radiative fluxes of the hot Jupiter HD179949b for which data from the Spitzer and Hubble Space Telescopes have been published (e.g., Burrows et al. 2008; Cowan et al. 2007). Physical and orbital parameters in Table 1 were employed to simulate the hot Jupiter. The parent star HD179949 is a F8V star, orbited by HD179949b at $0.0443 \pm 0.0026$ AU placing it among the closest orbiting planets in a low-eccentricity (e=$0.022 \pm 0.015$) orbit. The scattering parameter in the PHOENIX models was set to $\epsilon = 10^{-4}$ which could be a reasonable value to simulate a strong scattering environment. To get the radiative fluxes, it is assumed that, for irradiated atmospheres, the parent star is located at the zenith over the substellar point, that is, $\theta = \pi/2$ and $\phi = \pi$, where $\theta$ corresponds to the polar angle and $\phi$ to the azimuth angle. In this case, the day-night boundary is at $\theta = 0$. That is, the parent star is above the substellar point, 'above' means in the vertical direction assuming no axial tilts. The PHOENIX models assume circular orbits, which is a good approximation for most exoplanets in tight orbits.

The first experiment in this subsection corresponds to 3D cloud free radiative fluxes for the hot Jupiter HD179949b. The irradiated planets in this study have been modeled for two extreme cases: one where dust clouds form and remain suspended in the atmosphere (dusty models), and another where dust clouds form but completely settle out of the atmosphere (cloud free models). In the cloud-free situations, dust grains form in the atmosphere at locations determined by the chemical equilibrium equations but their opacity contribution is ignored, mimicking a complete removal of the grains by efficient gravitational settling. Therefore, those models represent cloud free atmospheres. In thay way, the cloud-free models may be thought of as clear skies, and the dusty model as cloudy skies.

Green curves in Figure 3 correspond to the Global Circulation Model, here also called the 1DRT Two-Stream model and black curves to the irradiated planet HD179949b modeled with PHOENIX, also called the 3DRT PHOENIX model. Plots show the radial and angular components of the flux vector ($F_r$, $F_\theta$ and $F_\phi$) versus wavelength. Figure 3 shows radiative fluxes at the substellar and antisubstellar points. That is, it does not show flux vectors across all outermost voxels (outermost radius, all ($\theta$, $\phi$) points). In the outermost voxels the pressure is equal to 0.002 mbar; temperature is equal to 880 K at the substellar point and 300 K at the antisubstellar point. Figure 3 shows cloud free fluxes in the 5000 - 150000 Å wavelength range, left frame corresponds to the substellar point and right frame to the antisubstellar point; these cloud free models do include TiO and VO opacities. The 3D radiative fluxes are medium resolution calculations, covering a broad wavelength range and placing the overall features in context, while models at high resolution are needed to identify specific absorption features.

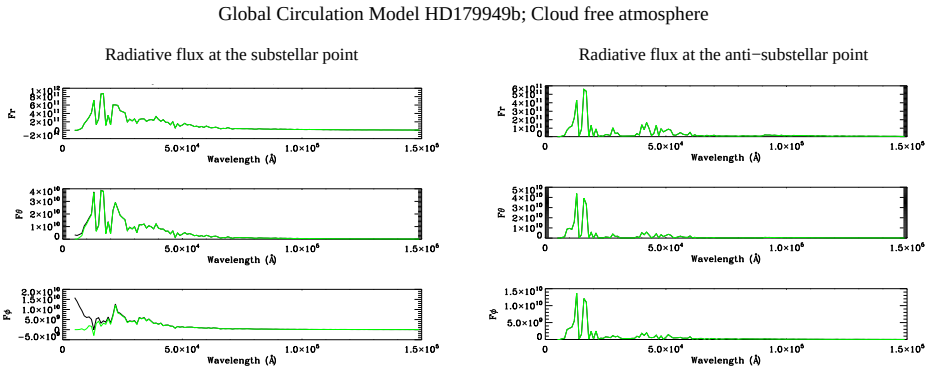
Global Circulation Model HD179949b; Cloud free atmosphere
Radiative flux at the substellar point
Radiative flux at the anti−substellar point
Wavelength (Å)

Fig. 3. 3D cloud-free radiative fluxes of the hot Jupiter HD179949b in the 5000 - 150000 Å wavelength range. Green curves correspond to the 1DRT Two-Stream model and black curve to the 3DRT PHOENIX model. Irradiated atmospheres on the day side remain very transparent and allow large amounts of flux to emerge from the deep hotter layers. Nightside spectra at the antisubstellar point show deep absorption bands of $H_2O$, CO, and/or $CH_4$; the 1DRT Two-Stream model dominates the nightside regime.

According to Figure 3, models on the day side show that in the 5000 - 15000 Å wavelength range the irradiated flux is larger than the emission by the 1DRT Two-Stream model, this is noted in the $F_\theta$ and $F_\phi$ flux components. Significant modulations present in the near-IR spectrum are best explained by the presence of water vapor and the carbon bearing molecules. The 3DRT PHOENIX model reflects a considerable amount of radiation in the optical bands compared to the 1DRT Two-Stream model. In models on the night side molecules predominate in the fluxes. At the anti-substellar point absorption features are created by molecules that could survive lower temperatures. The PHOENIX radiative fluxes in the near-IR contain significant modulations, which can be attributed to the presence of molecular bands seen in absorption. These are water ($H_2O$), carbon monoxide (CO), and carbon dioxide ($CO_2$) bands.

The $H_2O$ and $CH_4$ molecules have already been inferred for some hot Jupiters via transmission photometry and spectroscopy (e.g. Desert et al. 2009, Deming et al. 2013, Gibson et al. 2012, Sing et al. 2009, Birkby et al. 2013). Recently Madhusudhan et al. (2014) report conclusive measurements of $H_2O$ in the hot jupiter HD209458b, indeed they report the most precise $H_2O$ measurement in an exoplanet to date that suggests a $\sim$20-135$\times$sub-solar $H_2O$ abundance; and CO, thermochemically the most stable carbon molecule on the hot day-side, has been inferred from photometry (Barmam 2008; Charbonneau et al. 2008). The light reflected in the optical regime could be due to Rayleigh scattering by the two most abundant species, $H_2$ and He (Lecavelier des Etangs et al. 2008).

By modeling radiative fluxes at different positions on the planet, it is possible to see that the night side is in most cases equal to the same voxels in the 1DRT Two-Stream model, with the exception of the places where the light from the star shines through. Voxels that are identical (same fluxes) are not directly affected by the light from the star, the others are directly affected (and carry information about the atmosphere to the observers when the planet is transiting the stellar disk). Figure 3 illustrates how molecular opacities dominate the spectral range through which the planet radiates the bulk of their emergent flux ($\sim$ 15000 Å) leaving practically no window of true continuum. Models show molecular absorption features in the 10000 - 30000 Å wavelength range. Irradiated atmospheres on the day side remain very transparent and allow large amounts of flux to emerge from the deep hotter layers. Nightside fluxes at the antisubstellar point show deep absorption bands of $H_2O$, CO, and/or $CH_4$. In chemical equilibrium, CO would dominate over $CH_4$ across much of the dayside, but $CH_4$ dominates on the nightside. Molecular absorptions, primarily due to water and methane, are visible for $>$ 10000 Å. That is, the methane absorption probes the deeper layers and the water bands probe the upper layers and are sensitive to the irradiation.

The second test experiment in this subsection shows the effect by the presence of dust in the atmosphere of HD179949b. These cloudy models refer to the case when dust forms in the atmosphere at locations determined by chemical equilibrium equations. It is known that the forming dust clouds provide an enormous opacity and that condensating solid particles as clouds or haze layers can have strong opacities (e.g. Jones & Tsuji 1997). Because of this, it is expected that the spectral appearance of the object will be considerably changed, because clouds effectively reflect impinging radiation. The dusty models with PHOENIX exhibit a complex mixture of cloud species throughout the atmosphere. According to Barman et al. (2001), Fe, $Mg_2SiO_4$ and $MgSiO_3$ are the most prominent species except for the deeper layers where $CaMgSi_2O_6$ begins to dominate. Specifically, he argues that in the dusty models, Fe, $Mg_2SiO_4$, $MgSiO_3$, $CaMgSi_2O_6$ and $MgAl_2O_4$ are dominant dust species which form a cloudy region extending from roughly $\tau_{std} = 1.0$ to the top of the atmosphere, below this region ($\tau_{std} > 1.0$) is a mixture of various other condensates. To include dust grains, I have assumed an interstellar

size distribution with diameters ranging from 0.00625 to 0.24 microns and the chemical equilibrium equations incorporate over 1000 liquids and crystals, details in Barman et al. (2001) and Allard et al. (2001). Within the dusty calculations, the number densities for each grain species were calculated using the method of Grossman (1972) and the Gibbs free energies of formation from the JANAF database (Chase et al., 1985). Spherical shapes of the grains in this work are presented for simplicity. The effects of grain sizes and dust porosity on models are not explored in this study. Figure 4 presents dusty models at two positions on the planet; left frames correspond to fluxes at the substellar point and the right frames to fluxes at the antisubstellar point.

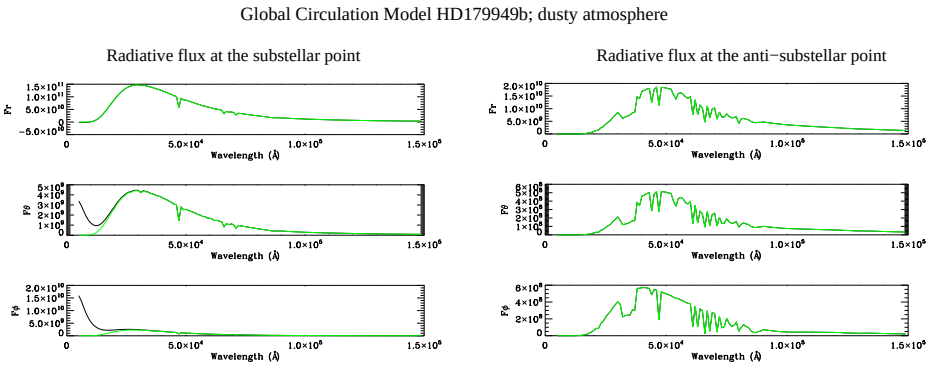
Global Circulation Model HD179949b; dusty atmosphere
Radiative flux at the substellar point
Radiative flux at the anti−substellar point
Wavelength (Å)

Fig. 4. Same description as Figure 3 but for models with dust opacity. Dust opacity generally produces a hotter atmosphere at all depths with a smoother spectral energy distribution. Absorption features are more prominent on the night side than on the day side. On the day side, the strong heating effects of dust opacities prevent the formation of methane bands, and $H_2O$ is dissociated while producing a hotter water vapor opacity profile, which is much weaker and more transparent to radiation.

On the day side, the strong heating effects of dust opacities prevent the formation of methane bands, and $H_2O$ is dissociated while producing a hotter water vapor opacity profile, which is much weaker and more transparent to radiation. The dusty absorption features are more prominent at the antisubstellar point than at the stellar point. The dusty model generates a very smooth flux in the optical, as expected, for an atmosphere dominated by grain opacity. In general, cloud free models are much brighter than the dusty cases because the dust opacity blocks most of the thermal radiation. In dayside models, for wavelengths shorter than $\sim$ 2000 Å, the reflected light in the dusty model matches closely the stellar light. The reflected light in the dusty models could be due almost entirely to Mie scattering which is a fairly grey process.

The radiative fluxes plotted in Figures 3 and 4 show flux vectors at one specific outermost voxel, that is, they do not show the flux vectors of all outermost voxels (outermost radius, all ($\theta$, $\phi$) points). Figure 5 shows radiative fluxes across the outermost voxels for the 1DRT Two-Stream (left) and 3DRT PHOENIX (right) models with clear skies. Models are shown in spherical coordinate systems. The radial component of the flux vector $F_r$

is the only non-zero component as in spherical symmetry both $F_\theta$ and $F_\phi$ are zero. The error in the angular components at short wavelengths of the 3DRT PHOENIX calculations can be due to the number of solid angle points. Hauschildt & Baron (2006, 2010) affirm that if the number of solid angle points with PHOENIX is too small, then $F_\theta$ and $F_\phi$ could have errors. They found that the higher solid angle resolution reduces the errors in $F_\theta$ and $F_\phi$ considerably and the higher internal accuracy due to more solid angle points also increases the internal accuracy of $F_r$.

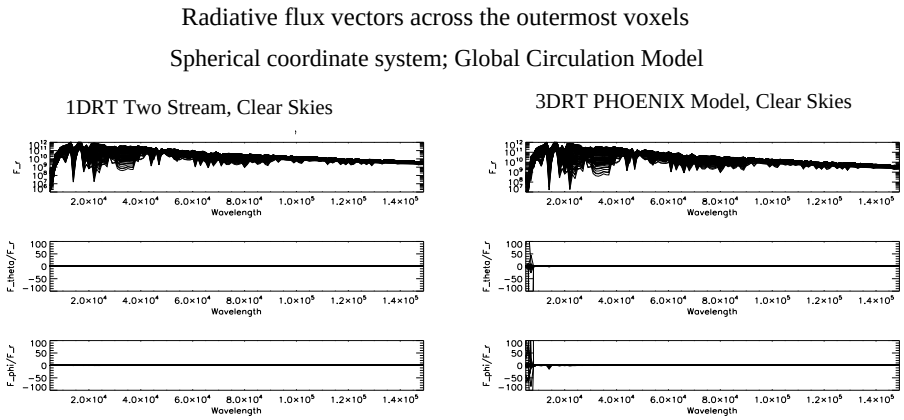


Fig. 5. Radiative flux vectors across the outermost voxels for the 1DRT Two-Stream (left) and 3DRT PHOENIX (right) Models with clear skies. Models are shown in spherical coordinate systems. Calculations use a 3D spherical coordinate system with $n_r$ = 53, $n_\theta$ = 257 and $n_\phi$ = 257 voxels for a total of about 3.5M voxels. The $F_r$ panels show the radial component of all outer voxels in logarithmic scale. The bottom panels show the corresponding runs of $F_\theta/F_r$ and $F_\phi/F_r$, respectively. They should be identically zero and the deviations measure the internal accuracy. The wavelengths are given in angstroms and the fluxes are in cgs units.

The third experiment in this subsection shows a 3D visualization of the irradiated Global Circulation Model to view spectro-images of the emitted mean intensities. The visualization reads the results of the 3D radiative transfer, perform a formal solution for a specific ($\theta$,$\phi$) and displays the results as images of the intensities. The 3D visualizations draw on the Global Circulation Model described in subsection 2.2 and show the influence of Atmospheric Dynamics on infrared radiative fluxes. Figure 6 shows wavelength resolved images of HD179949b for eight 45-degree phase increments. Frames show mean intensities in the 0.51-0.99 $\mu$m wavelength range (near infrared band). These kinds of visualizations could be a good step forward for the computational imaging of extrasolar planets. The slight pixellation and asymmetries are due to spatial and angular resolution.

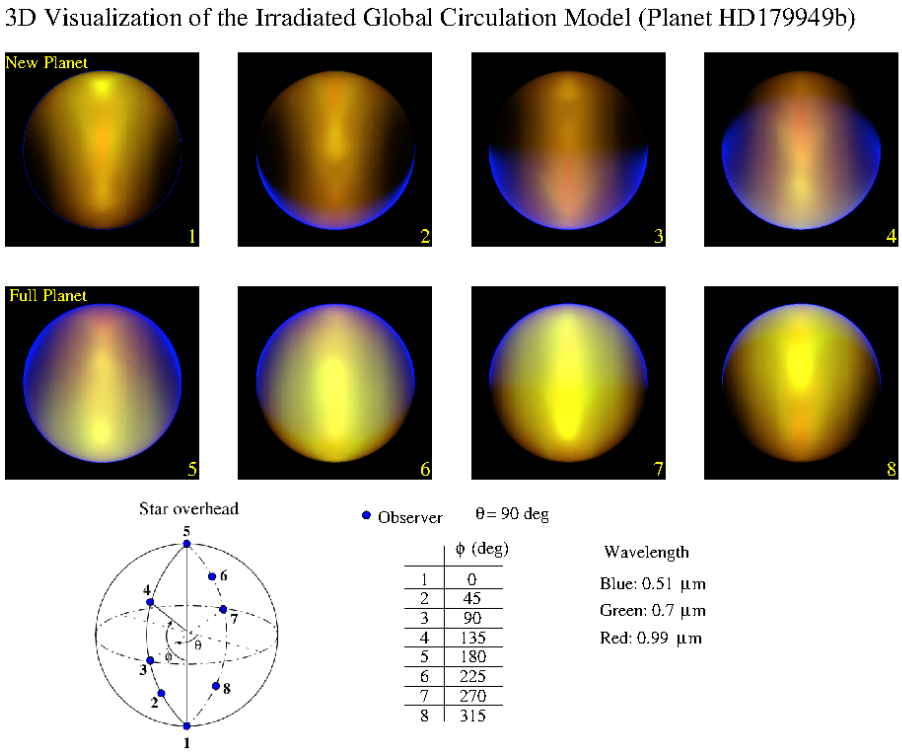


Fig. 6. Visualizations of the results for multi-wavelength 3D radiation transfer for a global circulation planetary atmosphere model for eight 45-degree phase increments in the planet HD179949b. The red channel corresponds to 0.99 $\mu$m, the green channel to 0.7 $\mu$m and the blue channel to 0.51 $\mu$m. The irradiated 1DRT Two-Stream model predicts a day side that is very similar to a blackbody, leading to a whitish appearance. On the night side, which is fairly cool, strong methane absorption knocks out the blue and green, leaving only red. Spectro-images directly map the patchy global patterns inferred to exist from models of multiwavelength variability.

In Figure 6 a bright near-sub stellar region can clearly be seen in the New Planet panel, the lightest and darkest regions shown correspond to brightness variations. A natural explanation for the features seen in Figure 6 is that spectro-images are directly mapping the patchy global patterns inferred to exist from observations and models of multiwavelength variability. The spectra of hot Jupiters vary strongly over their surface as the effects of irradiation will extremely vary over the surface; such effects are in principle observable through high-precision photometric and spectroscopic studies.

### 3.2. *Light Curves*

In this subsection theoretical light curves as function of wavelength for HD179949b have been calculated and confronted with actual measurements by the Spitzer Space Telescope. The observational data for the 8 $\mu$m light curve of HD179949b were taken from the Burrows et. al (2008) work (Figure 7 there), just from them. That Figure 7 portrays a comparison between their theoretical models for various combinations of parameters with the eight

observational data points of Cowan et al. (2007). The PHOENIX models simulate planetary transits, for each time step, 360 in total, a summation (addition) over all voxels over the planetary sphere gives the full intensity integration. Then the intensity integration is used to generate the PHOENIX light curves. The Global Circulation Model (hot Jupiter) passing in front of its parent star is simulated with PHOENIX on a 257x257 pixels grid. The PHOENIX models assume circular orbits, which is a good approximation for most exoplanets in tight orbits. Figure 7 presents theoretical light curves in the infrared regime. It shows planet-star flux ratios, left and right panels correspond to models for the cloud-free and dusty atmospheres, respectively. Within each panel, moving from top to bottom, light curves correspond to wavelengths from 13 $\mu$m to 2 $\mu$m.

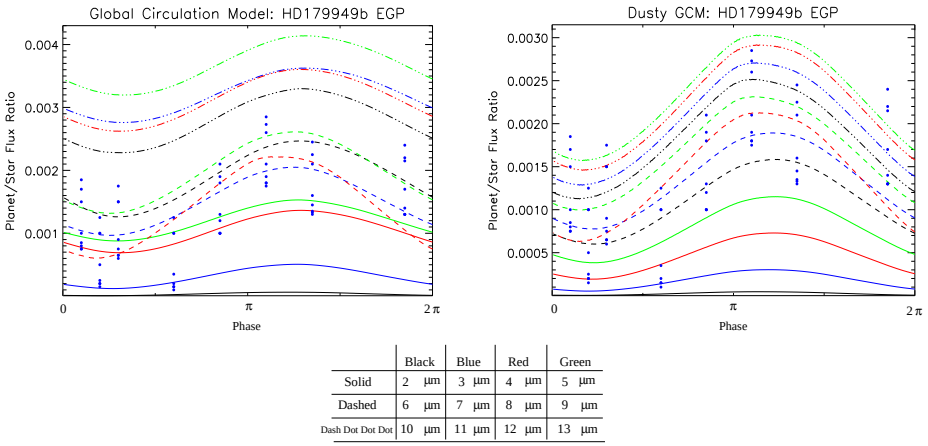


| | Black | Blue | Red | Green |
|---|---|---|---|---|
| Solid | 2 μm | 3 μm | 4 μm | 5 μm |
| Dashed | 6 μm | 7 μm | 8 μm | 9 μm |
| Dash Dot Dot Dot | 10 μm | 11 μm | 12 μm | 13 μm |

Fig. 7. Theoretical light curves in the 2.0-13.0 $\mu$m wavelength range for HD179949b. Left and right panels show cloud-free and dusty light curves, respectively. Within each panel, moving from top to bottom, the light curves are for wavelengths from 13 $\mu$m to 2 $\mu$m. Blue dots correspond to the 8 $\mu$m data points by Burrows et al. (2008). Light curves reach their peak flux after the secondary eclipse. These phase offsets result directly from the atmospheric dynamics of the 1DRT Two-Stream model.

Light curves in Figure 7 reach their peak flux after the secondary eclipse, a feature shared by all light curves. These phase offsets result directly from the atmospheric dynamics in the 1DRT Two-Stream model. According to Burrows et al. (2008), this may be a feature of a hot Jupiter with stratosphere and/or hot upper atmospheres. The shape and magnitude of the PHOENIX light curves strongly depend on the Rayleigh scattering of light from the host star, the presence of dust, the refraction of the stellar surface brightness distribution, and the optical depth through the planet's atmosphere, as determined by molecular opacity and clouds.

Then, the 8 $\mu$m cloud-free and dusty PHOENIX light curves were compared to the published 8 $\mu$m data points by Burrows et al. (2008). The theoretical and observational data are shown in Table 2, first column corresponds to the orbital phase; second and third columns to the PHOENIX planet-star

Flux ratios for the cloud-free ($R_{cf}$) and dusty ($R_d$) light curves, respectively and fourth column ($R_{obs}\pm\sigma$) to the observational data and uncertainties of Burrows et al. (2008).

TABLE 2

PLANET-STAR FLUX RATIOS AND OBSERVATIONAL DATA FOR HD179949B ($R_{OBS}$), THE THEORETICAL PREDICTIONS CORRESPOND TO CLOUD-FREE ($R_{CF}$) AND DUSTY ($R_D$) MODELS.

| Phase | Cloud Free ($R_{cf}$) | Dusty ($R_d$) | Data ($R_{obs}\pm\sigma$) |
|---|---|---|---|
| 0.1 | 0.00065 | 0.00065 | 0.00125±0.0005 |
| 0.2 | 0.00061 | 0.00065 | 0.00075±0.00055 |
| 0.3 | 0.00068 | 0.00073 | 0.001175±0.000575 |
| 0.6 | 0.00122 | 0.00126 | 0.00065±0.00055 |
| 0.85 | 0.0018 | 0.00179 | 0.0015±0.0005 |
| 1.1 | 0.00221 | 0.00213 | 0.002375±0.000625 |
| 1.35 | 0.00213 | 0.00203 | 0.001875±0.000625 |
| 1.85 | 0.00104 | 0.00102 | 0.001875±0.000625 |

The chi-square statistics is defined by

$$\chi^2 = \sum_{i=1}^{N} \frac{(R_{cf} - R_{obs})^2}{{\sigma_i}^2} \tag{1}$$

where the $\sigma_i$ is the uncertainty of each data point and $N$ is the number of independent variables. Ideally, given the values of $R_{cf}$ (or $R_d$) about their mean values $R_{obs}$, each term in the sum will be of order unity. The degrees of freedom $\nu$ are equal to 7, because there are $N$=8 data points and one adjustable parameter. It is found that the reduced $\chi^2$ is equal to 1.24 for the cloud-free model and to 1.27 for the dusty model, respectively. It would have had to have found the reduced $\chi^2$ in the vicinity of 1.0 to have been justified in suspecting the consistency of the measurements. Discrepancies are discussed in the discussion section.

### 3.3. *Reflection Spectra*

The basic tenet of the PHOENIX reflection spectra method is that the planet atmosphere absorption features are calculated as the stellar flux passes through the planet's atmosphere above the limb. The orbital phase for the PHOENIX reflection simulations is when the planet is fully projected on the visible hemisphere of the star so that the planet's projected transparent atmosphere takes out the greatest area and limb darkening from the star is at its minimum. By integrating the emergent intensities along an observer's line-of-sight for the observer-limb-star orientation, the flux passing is calculated through a section of a sphere encompassing the limb, in which case, rays entering at different latitudes will pass through different amounts of the planet's atmosphere. The theoretical reflection spectra for the hot Jupiter HD179949b are shown in Figure 8, there upper frames correspond to the stellar radiation

through the planet's atmosphere and bottom panels to the planet-star flux ratios. Left frames correspond to cloud-free atmospheres and right frames to dusty atmospheres, respectively.

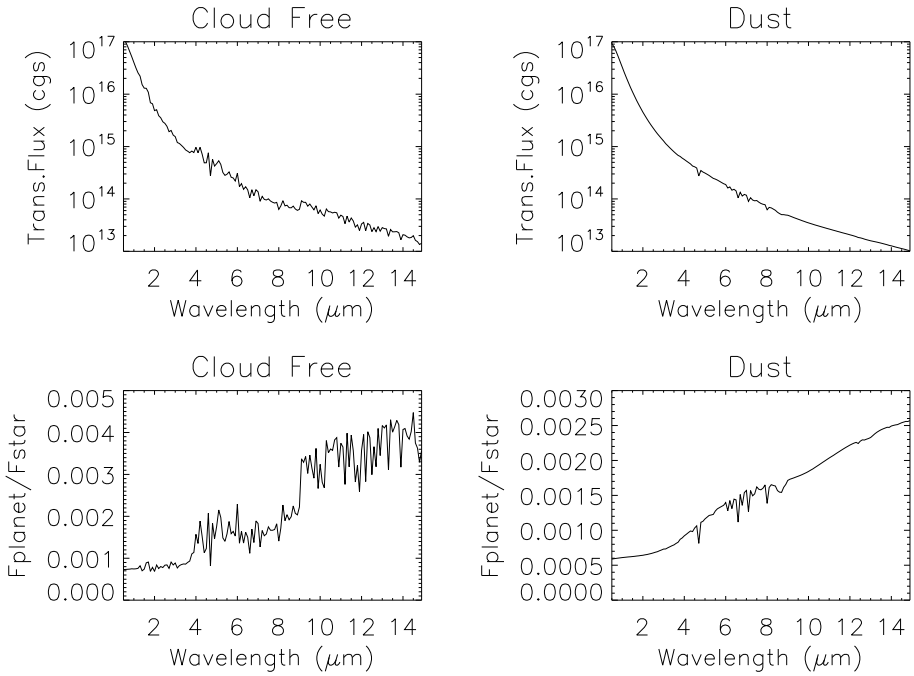


Fig. 8. 3D PHOENIX reflection spectra of the Planet HD179949b. Left frames correspond to cloud-free atmospheres whereas right frames to dusty atmospheres. Upper frames correspond to the stellar radiation through the planet's atmosphere, picking up some spectral features from the planet atmosphere and lower frames to the planet-star flux ratios. The cloud-free spectrum shows prominent $H_2O$ molecular absorption features. Absorption features by dust opacities are smaller than the molecular absorption feautures.

The PHOENIX atmospheres impose features on the spectra of its parent star during transit; these features contain information about the physical conditions and chemical composition of the atmospheres. In the cloud-free spectrum, most prominent molecular absorption features are seen from ∼4 $\mu$m to 14 $\mu$m. This spectrum shows prominent $H_2O$ molecular absorption features. In dusty models, the most prominent absorption features are noted in the 4.5-9 $\mu$m wavelength range, the 0.5-4.5 $\mu$m and 9-14 $\mu$m wavelength ranges are featureless. Absorption features by dust are smaller than the molecular absorption feautures. Many important optical/near-IR molecular opacity sources (TiO and VO) have been completely removed by the dust formation. It is also found that the apparent radius of the planet in the optical regime is equal to 0.12 $R_{star}$, which is in agreement with predictions in the literature (i.e. Wang & Ford 2011), the apparent radius is calculated following analysis of Seager (2010).

Then, the 3D PHOENIX reflection spectrum for HD179949b is confronted

with the Spitzer secondary-eclipse photometry of Knutson et al. (2008, 2009). The planet HD209458b was chosen to be confronted with the PHOENIX model because it has similar orbital parameters to the hot Jupiter HD179949b. The planet HD209458b is also interesting in terms of reflection spectroscopy because of the presence of molecules such as $CH_4$, CO and $H_2O$ (Barman 2008; Swain et al. 2008). Table 3 contains the observational planet-star flux ratios for HD209458b and the PHOENIX predictions for HD179949b; Figure 9 shows the 3D PHOENIX cloud-free reflection spectrum of HD179949b and in red error bars the observational data of Showman et al. (2009) for the hot Jupiter HD209458b.

TABLE 3

PHOENIX PLANET-STAR FLUX RATIOS FOR HD179949B AND THE OBSERVATIONAL DATA FOR HD209458B ($R_{OBS}$).

| Planet-Star flux ratios ($F_P/F_S$)(%) | 3.6 $\mu$m | 4.5 $\mu$m | 5.8 $\mu$m | 8.0 $\mu$m |
|---|---|---|---|---|
| HD209458b ($R_{obs}$) | 0.094±0.009 | 0.213±0.015 | 0.301±0.043 | 0.240±0.026 |
| PHOENIX model for HD179949b | 0.1044 | 0.14152 | 0.19024 | 0.174 |

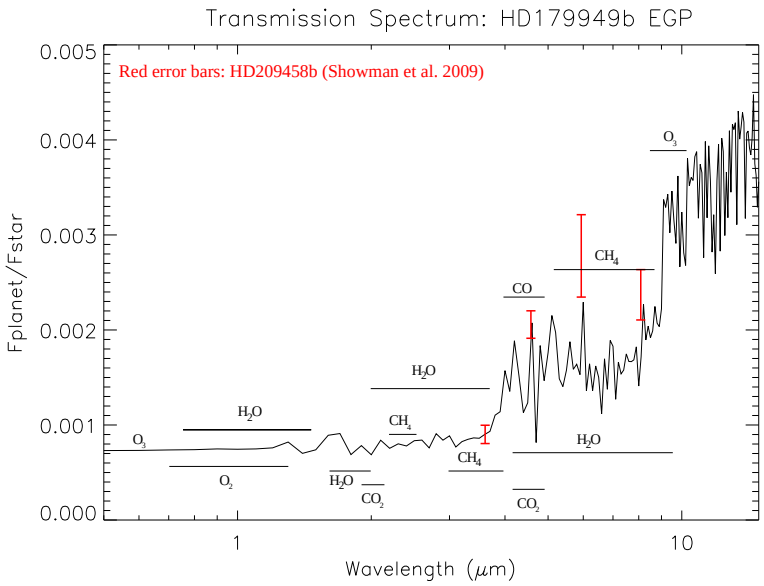


Fig. 9. Cloud-free reflection spectrum for the planet HD179949b. Absorption of visible and near IR radiation in the gaseous atmosphere are primarily due to $H_2O$, $O_3$, and $CO_2$, the main atmospheric gases absorbing/emitting in the IR are: $CO_2$, $H_2O$, $O_3$, $CH_4$, $N_2O$. In red error bars are those observational data for the hot Jupiter HD209458b. The PHOENIX model matches the secondary-eclipse depths at 3.6 $\mu$m, however, it underpredicts the eclipse depths at 4.5, 5.8 and 8.0 $\mu$m.

Figure 9 shows important absorption features, the most useful diagnostics are likely to be the near-infrared bands of molecules, and the visible/near-IR resonance lines of the alkali metals (Barman et al. 2005; Burrows et al. 2008).

In general, the cloud-free reflection spectrum in the mid infrared is sensitive to molecular abundances. The strengths of molecular lines provide diagnostics for the temperature, and the vertical temperature structure. On the other hand, it is found that the $\chi^2$ is equal to 37.12 and the reduced $\chi^2$ to 12.37 with 3 degrees of freedom. The PHOENIX spectrum in Figure 9 matches the secondary-eclipse depth at 3.6 $\mu$m, however, it underpredicts the eclipse depths at 4.5, 5.8 and 8.0 $\mu$m. When a spectrum exhibits greatly differing brightness temperatures at different wavelengths (as in case of HD209458b), a common explanation is that the different wavelengths sense different pressure levels (because of the wavelength-dependent opacities) (e.g. Cubillos et al. 2013). In this context, the fundamental stumbling block to simultaneously explain the four Spitzer secondary-eclipse depths is that the range of pressures that the photons contribute to the 3.6, 4.5, 5.6, 8.0 $\mu$m wavelengths are all very similar at least for the radiative-transfer PHOENIX model, chemical composition, and opacities adopted for the model. Thus, it is difficult to produce a high brightness temperature in some bands (such as at 4.5 $\mu$m, 5.8 $\mu$m and 8$\mu$m) while maintaining low brightness temperature in other bands (such as at 3.6 $\mu$m) as the data apparently require. The temperature discrepancy problem is not confined to the present study.

## 4. DISCUSSIONS AND CONCLUSIONS

In this work spectra and light curves of a detailed Global Circulation Model (GCM) in the presence of a strong impinging radiation from its parent star have been presented and compared to actual observations in the infrared regime. The GCM uses radiative-equilibrium temperatures as a function of longitude, latitude, and pressure; then the Temperature-Pressure structures are employed as input structure files to feed the 3D planetary atmosphere PHOENIX code. The incorporation of a realistic 3D radiative transfer code represents the relevance of this work in the development of hot jupiter atmospheres.

Radiative fluxes for the hot Jupiter HD179949b were calculated at the substellar and anti-substellar points to look for differences. Models on the day side show that the flux by the 3DRT PHOENIX code is larger than the emission by the 1DRT Two-Stream model in the 5000 - 15000 Å wavelength range. Nightside fluxes at the antisubstellar point show deep absorption bands of $H_2O$, CO, and/or $CH_4$. Dusty models on the day side show that the strong heating effects of dust opacities prevent the formation of methane bands, and $H_2O$ is dissociated while producing a hotter water vapor opacity profile, which is much weaker and more transparent to radiation. The dusty absorption features are more prominent at the antisubstellar point than at the stellar point. The dusty model generates a very smooth flux in the optical as it is expected for an atmosphere dominated by grain opacity.

Theoretical light curves as a function of wavelength for the hot Jupiter HD179949b were calculated and compared to actual observational data by the Spitzer Space Telescope. The PHOENIX simulations explain the broad

features of the observed 8.0 $\mu$m light curves (Cowan et al. 2007, Burrows et al. 2008), including the fact that the planet-star flux ratio peaks before the secondary eclipse. PHOENIX radiative fluxes and phase-dependent light curves, reveal the molecular and atomic compositions, atmospheric temperatures and the degree to which the radiation on the day side is redistributed to the night side.

The PHOENIX cloud free reflection spectrum was confronted with actual data points from the Spitzer Telescope for the Jupiter HD209458b. The theoretical predictions provides reasonable matches to the Spitzer secondary-eclipse depth at 3.6 $\mu$m, however, it underpredicts the eclipse depths at 4.5, 5.8 and 8.0 $\mu$m. These discrepancies result from the chemical composition.

The majority of the problems that the results have matching the data to the spectrum and light curves are not due to the PHOENIX calculations but is rather due to the global circulation calculations. Particularly, we are aware that better global circulation models exist and have indeed been developed because of the limitation of the newtonian cooling and its unability to fit the observations. The GCM used in this work was created to simulate the hot Jupiter HD209458b, which has been a prototypical exoplanet for atmospheric thermal inversions (e.g. Showman et al. 2009), however this assertion does not take into account recently obtained data or newer data reduction techniques. Recently Diamond-Lowe et al. (2014) revised the value of the Spitzer measurements and found a very good agreement with the theory, they determined that it is unnecessary to invoke a thermal inversion to explain the secondary-eclipse depths. They concluded that there is no evidence for a thermal inversion in the atmosphere of HD 209458b. This suggests the PHOENIX models to select better circulation models for the hot Jupiter HD179949b. Another possibility is that there is still physics that is not included in the theoretical models which are causing the discrepancies.

These assignments require a work collaboration with other groups to produce one cohesive work. According to Diamond-Lowe et al. (2014), their group is working on exploring the effects of a wide range of planetary properties, including eccentricity, orbital distance, rotation rate, mass, gravity, composition, metallicity, and stellar flux on circulation models. Their work group could represent a suitable collaboration to calculate theoretical radiative fluxes, spectra and light curves of a variety of circulation models with the radiative transfer PHOENIX code. We expect that the high spectral resolution of JWST should enable meaningful inferences about atmospheric structure and composition of hot Jupiters. The JWST will be a powerful tool for exoplanet transit spectroscopy of a wide range of planets, due to its broad wavelength coverage and high sensitivity (Barstow et al. 2015).

Results presented in this study represent a first approach to a full and detailed analysis of 3D spectra and light curves of hot Jupiters. The relatively low resolution models presented here, covering a broad wavelength range, place the overall features in context, while models at medium or high resolution could be much better suited to identify specific absorption features

and probe planetary atmospheres over a large pressure range.

Finally I conclude that there is a significant amount of work to be done, it is especially crucial that better circulation models, high resolution calculations, and full integrated radiative fluxes are planned well in advance. Here we identify these specific areas for necessary future work within the PHOENIX group.

## 5. ACKNOWLEDGEMENTS

Author thanks the Graduiertenkolleg (GrK) 1351 Extrasolar Planets and their Host Stars fellowship granted by the Deutsche Forchunsgemeinschaft. He is greatly grateful to the Hamburger Sternwarte of the University of Hamburg, Germany for a fruitful stay where this work got started.

## REFERENCES

Allard, F., Hauschildt, P. H., Alexander, D. R., Tamanai, A., & Schweitzer, A. 2001, ApJ, 556, 357

Barman, T. S. 2008, ApJ, 676, L61

Barman, T. S., Allard, F., Baraffe, I., Chabrier, G., & Hauschildt, P. H. 2005, 13th Cambridge Workshop on Cool Stars, Stellar Systems and the Sun, 560, 437

Barman, T. S., Hauschildt, P. H., & Allard, F. 2001, ApJ, 556, 885

Barman, T. S., Hauschildt, P. H., Schweitzer, A., et al. 2002, ApJ, 569, L51

Baron, E., Chen, B., & Hauschildt, P. H. 2009, American Institute of Physics Conference Series, 1171, 148

Baron, E., & Hauschildt, P. H. 2007, A&A, 468, 255

Barstow, J. K., Aigrain, S., Irwin, P. G. J., Kendrew, S., & Fletcher, L. N. 2015, MNRAS, 448, 2546

Birkby, J. L., de Kok, R. J., Brogi, M., et al. 2013, MNRAS, 436, L35

Burkert, A., Lin, D. N. C., Bodenheimer, P. H., Jones, C. A., & Yorke, H. W. 2005, ApJ, 618, 512

Burrows, A., Budaj, J., & Hubeny, I. 2008, ApJ, 678, 1436

Burrows, A., Sudarsky, D., & Hubeny, I. 2006, ApJ, 650, 1140

Burrows, A., Rauscher, E., Spiegel, D. S., & Menou, K. 2010, ApJ, 719, 341

Cannon, C. J. 1973, J. Quant. Spec. Radiat. Transf., 13, 627

Charbonneau, D., Knutson, H. A., Barman, T., et al. 2008, ApJ, 686, 1341

Chase, M. W., Davis, C. A., Downey, J. R., Frurip, D. J., McDonald, R. A., & Syverud, A. N. 1985, J. Phys. Chem. Ref. Data, 14, 1

Cho, J. Y.-K., Menou, K., Hansen, B. M. S., & Seager, S. 2003, ApJ, 587, L117

Cooper, C. S., & Showman, A. P. 2005, ApJ, 629

Cowan, N. B., Agol, E., & Charbonneau, D. 2007, MNRAS, 379, 641

Cubillos, P., Harrington, J., Madhusudhan, N., et al. 2013, ApJ, 768, 42

Deming, D., Harrington, J., Seager, S., & Richardson, L. J. 2006, ApJ, 644, 560

Deming, D., Wilkins, A., McCullough, P., et al. 2013, ApJ, 774, 95

Désert, J.-M., Lecavelier des Etangs, A., Hébrard, G., et al. 2009, ApJ, 699, 478

Diamond-Lowe, H., Stevenson, K. B., Bean, J. L., Line, M. R., & Fortney, J. J. 2014, ApJ, 796, 66

Dobbs-Dixon, I., & Agol, E. 2013, MNRAS, 435, 3159

Fortney, J. J., Shabram, M., Showman, A. P., et al. 2010, ApJ, 709, 1396
Gibson, N. P., Aigrain, S., Pont, F., et al. 2012, MNRAS, 422, 753
Grossman, L. 1972, Geochim. Cosmochim. Acta, 36, 597
Hauschildt, P. H. 1992, J. Quant. Spec. Radiat. Transf., 47, 433
Hauschildt, P. H., Barman, T., & Baron, E. 2008, Physica Scripta Volume T, 130, 014033
Hauschildt, P. H., & Baron, E. 1999, Journal of Computational and Applied Mathematics, 109, 41
Hauschildt, P. H., & Baron, E. 2006, A&A, 451, 273
Hauschildt, P. H., & Baron, E. 2010, A&A, 509, A36
Husser, T.-O., Wende-von Berg, S., Dreizler, S., et al. 2013, A&A, 553, A6
Iro, N., Bézard, B., & Guillot, T. 2005, A&A, 436, 719
Jones, H. R. A., & Tsuji, T. 1997, ApJ, 480, L39
Knutson, H. A., Charbonneau, D., Allen, L. E., Burrows, A., & Megeath, S. T. 2008, ApJ, 673, 526
Knutson, H. A., Charbonneau, D., Cowan, N. B., et al. 2009, ApJ, 690, 822
Knutson, H. A., Charbonneau, D., Noyes, R. W., Brown, T. M., & Gilliland, R. L. 2007, ApJ, 655, 564
Lecavelier Des Etangs, A., Pont, F., Vidal-Madjar, A., & Sing, D. 2008, A&A, 481, L83
Mihalas, D. 1978, San Francisco, W. H. Freeman and Co., 1978. 650 p.
Olson, G. L., & Kunasz, P. B. 1987, J. Quant. Spec. Radiat. Transf., 38, 325
Rauscher, E., & Menou, K. 2010, ApJ, 714, 1334
Scharmer, G. B. 1984, Methods in Radiative Transfer, 173
Seager, S. 2010, Exoplanet Atmospheres: Physical Processes. By Sara Seager. Princeton University Press, 2010. ISBN: 978-1-4008-3530-0,
Seager, S., Richardson, L. J., Hansen, B. M. S., Menou, K.; Cho, J. Y.-K.; Deming, D. 2005, ApJ, 632, 1122
Showman, A. P., & Guillot, T. 2002, A&A, 385, 166
Showman, A. P., Fortney, J. J., Lian, Y., et al. 2009, ApJ, 699, 564
Sing, D. K., Désert, J.-M., Lecavelier Des Etangs, A., et al. 2009, A&A, 505, 891
Smith, W., & Missen, R. 1982, in Chemical reaction equilibrium analysis: theory and algorithms, Wiley series in chemical engineering (Wiley)
Swain, M. R., Bouwman, J., Akeson, R., Lawler, S., & Beichman, C. 2008, ApJ, 674, 482
Wang, J., & Ford, E. B. 2011, MNRAS, 418, 1822

Juan J. Jiménez-Torres: Hamburger Sternwarte, Gojenbergsweg 112, 21029 Hamburg, Germany (jtorres@hs.uni-hamburg.de)